


Evidence of anomalous conventional and spontaneous exchange bias, high coercivity in Fe doped NiCr_2O_4 spinel[†]

G. C. Pandey,^a K. Nemkovski,^b Y. Su^b and Chandana Rath  ^{*a}

$\text{NiCr}_{2-x}\text{Fe}_x\text{O}_4$ ($x = 0$ and 0.2) polycrystalline ceramics have been synthesized successfully through a simple co-precipitation technique to study the evolution of structural and magnetic properties by doping Fe. X-ray diffraction (XRD) reveals that the high-temperature cubic phase (space group $Fd\bar{3}m$) observed at 320 K in bulk NiCr_2O_4 is stabilized at room temperature by decreasing the particle size to nanometer in $x = 0$ as well as after incorporating 20 at% Fe in the NiCr_2O_4 lattice. The cation distribution obtained from X-ray absorption fine structure (XAFS) analysis illustrates that while in $x = 0$, Ni^{2+} and Cr^{3+} ions occupy the tetrahedral (A) and octahedral (B) sites, respectively, $x = 0.2$, Fe^{3+} and Cr^{3+} ions occupy the A and B sites, respectively, and Ni^{2+} ions are distributed among the A and B sites. This transformation from the normal to mixed spinel structure strongly affects the magnetic properties. While the paramagnetic to long-range ferrimagnetic ordering temperature T_C is enhanced from 71 to 192 K, significantly large coercive field (H_C) of ~ 29 kOe is observed for $x = 0.2$ as compared to the $H_C \sim 13$ kOe for $x = 0$. Moreover, unusually large conventional and spontaneous exchange bias fields of ~ 26 and ~ 2.6 kOe are observed for $x = 0.2$, which is absent for $x = 0$. The presence of anomalous exchange bias field is ascribed to the unidirectional exchange anisotropy between the two magnetic sublattices at A and B sites. The training effect of the exchange bias field is discussed using a phenomenological model, which considers the contribution from irreversible uncompensated spins that modify the exchange anisotropy at the interface between A and B magnetic sublattices. In addition, diffuse neutron scattering (DNS) with XYZ analysis is employed for both compositions to clearly illustrate the low-temperature peculiar magnetic phase transitions such as spin spiral transition, T_S and spin lock-in transition, T_L . The DNS demonstrates that while T_L decreases from 10 K to 7 K with the incorporation of Fe in the NiCr_2O_4 lattice, T_S significantly increases from 28 K to 50 K.

Introduction

Chromites, with the general formula ACr_2O_4 ($A = \text{Ni}, \text{Co}, \text{Zn}, \text{Fe}, \text{etc.}$) have attracted much attention not only due to their potential applications that span from electronic and memory devices to electrode and catalysts materials but due to their multiferroic nature.^{1–3} At high temperature, these spinel compounds crystallize in the cubic phase with the space group $Fd\bar{3}m$, where oxygen ions form the face-centered cubic (FCC) lattice. Within this structure, there are two types of interstitial sites surrounded by oxygen ions such as the tetrahedral A site and the octahedral B site. While A^{2+} ion occupy the A site, Cr^{3+}

ion preferentially occupy the B site due to its large crystal field stabilization energy.⁴ The presence of orbital degeneracy in the A site ions, such as Ni^{2+} , Fe^{2+} , and Cu^{2+} , leads to the reduction of the high symmetry cubic phase into the tetragonal phase caused by cooperative Jahn–Teller distortion.⁵ Moreover, strong coupling between the spin, orbital, and lattice degrees of freedom in these compounds further enable the reduction of lattice symmetry coupled with magnetic phase transition.^{5,6} In this context, NiCr_2O_4 is a unique normal spinel compound that not only exhibits concurrent structural and magnetic phase transitions but is also reported to exhibit multiferroic properties.^{5–7} It undergoes a structural phase transition from the cubic to tetragonal (space group $I4_1/amd$) phase caused by cooperative Jahn–Teller distortion at 320 K.^{6,7} Below 320 K, magnetostructural coupling induced tetragonal to orthorhombic (space group $Fddd$) phase transition occurs at 65 K, which coincides with the Curie temperature, T_C .⁶ Further, distortion within the orthorhombic phase at spin-spiral ordering temperature, $T_S \sim 31$ K has been observed.^{8,9} Besides the intri-

^aSchool of Materials Science and Technology, Indian Institute of Technology (BHU), Varanasi, 221005, India. E-mail: chandanarath@yahoo.com

^bForschungszentrum Jülich GmbH, Jülich Centre for Neutron Science (JCNS) at Heinz Maier-Leibnitz Zentrum (MLZ), Lichtenbergstr. 1, 85748 Garching, Germany

[†]Electronic supplementary information (ESI) available. See DOI: 10.1039/d0dt00124d

guing structural and magnetic phase transitions, NiCr_2O_4 exhibits a complicated magnetic structure where A site magnetic ions form a diamond sublattice with the ferromagnetic (FM) ordering and Cr^{3+} ions occupies the B sites forming the magnetically frustrated pyrochlore sublattice with the antiferromagnetic (AFM) exchange interaction between neighboring Cr^{3+} ions.¹⁰ Thus, the incorporation of different transition elements in either A or B sites offers lots of opportunities for tuning the structural and magnetic properties such as the coexistence of structural phases, exchange bias (EB), large coercivity, and temperature induced magnetization reversal.^{11–13} For instance, EB has drawn significant attention due to its potential technological applications in spin valves, read heads for recording devices, and magnetic tunnel junction based devices.^{14–16} There are two different types of EB such as conventional exchange bias (CEB) and spontaneous exchange bias (SEB), which are manifested as the shift in the hysteresis loop along the magnetic field axis under the presence and absence of magnetic field cooling, respectively.^{17–19} These are generally induced by the unidirectional exchange anisotropy at the interface between irreversible and reversible magnetic phases. Meiklejohn and Bean have first reported the CEB in Co/CoO in 1956 and since then, it has been tremendously explored and studied in a large number of systems, including FM/AFM magnetic multilayers, FM-spin glass (SG) system, and FM/AFM nanocomposite structures.^{20–23} On the other hand, SEB was first observed by Wang *et al.* in 2011 in Ni-Mn-In based Heusler alloy and later on, it was mainly studied in three magnetic systems, including antiperovskite, Heusler alloy, and BiFeO_3 based composites.^{24–27} Recently, SEB of ~ 2.3 kOe has been reported in Cu doped CoCr_2O_4 spinel compound by Wang *et al.*, which they attributed to the exchange coupling interaction between the AFM and FM sublattices.²⁸ Similarly, Barman *et al.* showed that incorporation of non-magnetic Al in NiCr_2O_4 lattice leads to the development of anisotropic exchange interaction between FM and AFM sublattices, resulting in CEB of 2.83 kOe.²⁹ In addition, the presence of spin glass (SG) phase has been reported in Mn substituted NiCr_2O_4 by Zhu *et al.*, which consequently results in CEB of ~ 3.3 kOe and significantly large H_C of ~ 21 kOe.³⁰ In our recent report, we have demonstrated the presence of very large CEB and SEB of ~ 11 and 1.2 kOe, respectively, after doping 10 at% Fe in the NiCr_2O_4 lattice.¹¹ In order to further increase the CEB/SEB, we have further enhanced the Fe concentration in the NiCr_2O_4 nanoparticles.

In this report, we compare the structural and magnetic properties of NiCr_2O_4 and $\text{NiCr}_{1.8}\text{Fe}_{0.2}\text{O}_4$ to illustrate the role of Fe in NiCr_2O_4 . Unlike bulk NiCr_2O_4 , we observed the stabilization of the cubic phase at RT in both $x = 0$ and 0.2. XAFS analysis reveals that with incorporation of Fe, while Fe^{3+} and Cr^{3+} ions occupy A and B sites, respectively, and Ni^{2+} ions are distributed among A and B sites showing a mixed spinel structure. While normal to mixed spinel conversion enhances T_C from 72 K to 192 K, an anomalous increase in the coercivity of 29 kOe was observed for $x = 0.2$. Surprisingly, unusually high CEB ~ 26 kOe and SEB ~ 2.6 kOe have been observed for $x = 0.2$. The origin of

CEB/SEB is discussed in the context of irreversible uncompensated AFM spins at the B site, providing pinning force to the rotation of reversible FM spins at the A site. The validation of CEB and its origin is further understood through the training effect.

Experimental work

Synthesis procedure

$\text{NiCr}_{2-x}\text{Fe}_x\text{O}_4$ ($x = 0$ and 0.2) powder samples were prepared by the easy, cost-saving co-precipitation technique. Prior to the synthesis, separate 1 M stock solutions of ferric nitrate ($\text{Fe}(\text{NO}_3)_3 \cdot 9\text{H}_2\text{O}$), chromium nitrate ($\text{Cr}(\text{NO}_3)_3 \cdot 9\text{H}_2\text{O}$), and nickel nitrate ($\text{Ni}(\text{NO}_3)_2 \cdot 6\text{H}_2\text{O}$) were prepared. The required stoichiometric amounts of these nitrate solutions were mixed and subjected to magnetic stirring for 1 h, followed by the slow addition of aqueous ammonia solution of 1 M concentration. The addition of ammonia solution was continued till the pH of the mixed solution was 9. The obtained precipitate was filtered using filter paper (Whatman, Grade 1) and then washed several times using deionized water, followed by acetone. Afterwards, the precipitate was dried in an oven at 125 °C for 48 h and was properly crushed and grinded using a mortar and pestle to obtain the fine powders. Finally, the fine powders were calcined at 1100 °C for 6 h for better crystallinity.

Characterizations

The calcined powders were characterized by X-ray diffraction (XRD), scanning electron microscopy (SEM), X-ray absorption fine structure (XAFS) spectroscopy, diffuse neutron scattering (DNS), and magnetic measurements. XRD was carried out at RT using a Rigaku powder diffractometer in Bragg-Brentano θ - θ geometry with a fixed sample holder and a curved crystal graphite monochromator. A ZEISS scanning electron microscope (SEM, SIGMA) was used to carry out the microstructural analysis. The Cr, Fe, and Ni K-edge XAFS spectra were collected using the XAS beamline, Elettra-Sincrotrone, Trieste (Italy) in the transmission mode. The target materials were prepared by mixing the calcined powder thoroughly with polyvinylpyrrolidone $[(\text{C}_6\text{H}_9\text{NO})_n]$ in the ratio of 1:10 and the pellets of 15 mm diameter were made after applying 1 ton of pressure. The analysis of the XAFS spectra was performed using the Demeter package (Athena, Artemis, and Hephaestus) developed by B. Ravel and M. Newville in 2005.³¹ This Demeter package is based on the IFEFFIT program suite and coded in the Perl programming language with Perl/TK graphics toolkit, and also uses the PGPLOT package for plotting data. The package is free of cost and portable to various computer operating systems such as Windows, Linux, and Macintosh. Initially, the raw data were reduced to a suitable form using the Athena software, which includes the following operations: conversion of raw data into $\mu(E)$, background removal, data normalization, and main edge position (E_0) determination. E_0 refers to the energy value where the intensity of normalized

absorption was 0.5. The experimental data were fitted with the theoretical spectrum generated by the Atoms and FEFF programs inbuilt with the Artemis software. The diffuse neutron scattering (DNS) spectrometer at FRM II, JCNS, Garching, Germany was used to carry out the polarized neutron scattering (XYZ polarization analysis) of the $x = 0$ and 0.2 samples. The measurements were carried out by mounting the samples on aluminum holders with the sample environment of the top-loading closed cycle refrigerator (CCR) type in the temperature range of 3.5–180 K. Both horizontally and vertically adjustable monochromators with double focusing were used to select the neutron wavelength (4.2 Å). The separation of magnetic contribution from the spin-incoherent and nuclear coherent contributions was performed using XYZ-polarization analysis by the dnsplot software. A vibrating sample magnetometer (VSM) of quantum design was used for the temperature and magnetic field dependent dc magnetization measurements within the temperature range of 2–300 K and the maximum field range of –70 to 70 kOe. Before measurement, the coil was demagnetized in the oscillatory mode from –70 to +70 kOe at RT to remove any trapped magnetic flux in the superconducting coil.

XAFS analysis

Fig. 1(a–f) depicts the normalized X-ray absorption near-edge spectroscopy (XANES) spectra along with the pre-edge features measured at Ni, Cr, and Fe K-edges for $\text{NiCr}_{2-x}\text{Fe}_x\text{O}_4$ ($x = 0$ and 0.2). It has been reported that the pre-edge features are mainly due to the electronic transition between different shells and the intensity of the pre-edge peak strongly depends on the coordination geometry surrounding the absorbing atom.^{32–35} The intense pre-edge features are mostly observed for the absorbing atom present in a non-centrosymmetric environment such as an A site due to the sum of the significantly large electric dipole transition of 1s electron and the p component in 3d–4p hybridized metal orbitals and the very small electric quadrupole transition of 1s electron to the 3d orbital.^{32,33,36} Less intense pre-edge peaks are mostly observed in a centrosymmetric environment such as a B site where the 3d–4p hybridization is not possible, which leads to the only electric quadrupole (1s → 3d) transition.^{32–36} Prior to the analysis of the pre-edge feature, the background of the pre-edge peaks were subtracted using a spline function, which smoothly follows the data points prior and immediately after the pre-edge peak. Afterwards, the fitting of the pre-edge peak is performed using a Gaussian profile function for all the three transition metal K-edges in $x = 0$ and 0.2, as shown in Fig. 2. The results of the fitting are given in Tables 1–3. The pre-edge peak intensity is estimated as the product of normalized peak height and full-width at half maximum (FWHM) of the pre-edge peak (Tables 1–3).³⁷ The most intense pre-edge feature is observed at the Fe K-edge for $x = 0.2$ (Fig. 2). Similar results for pre-edge features at Fe K-edge have been reported by Wilke *et al.* where Fe^{3+} ion occupies the A site.³⁸ Also, an intense pre-edge peak has been reported for the distorted FeO_6 and TiO_6 octahedra in BaFeO_3 and BaTiO_3 perovskites at the Fe and Ti

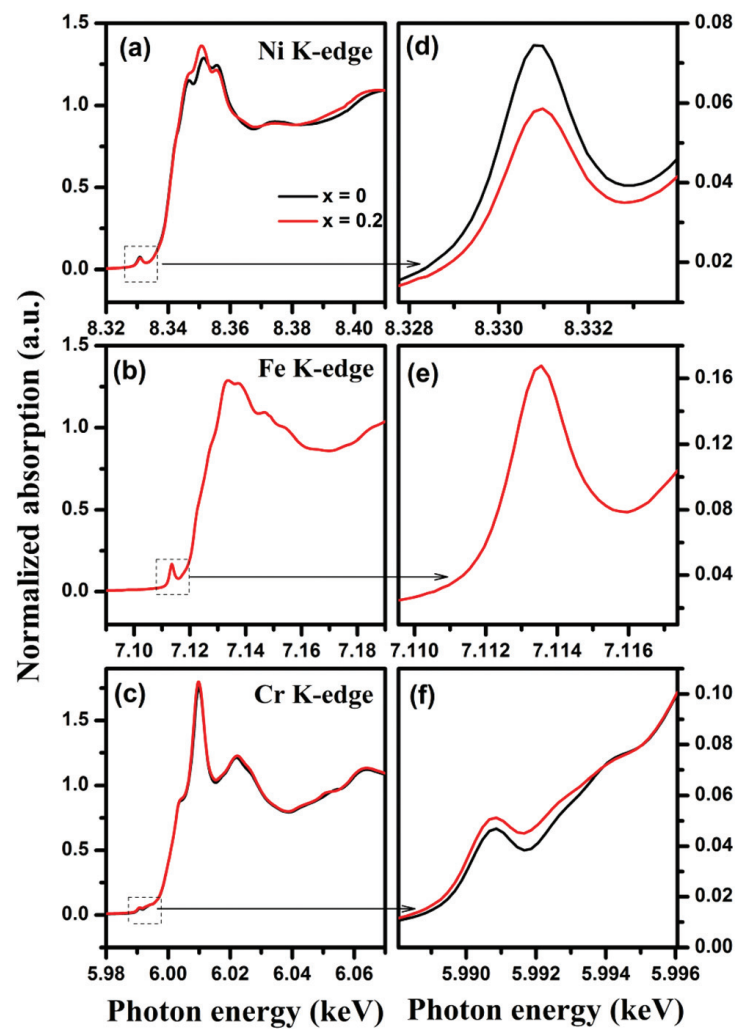


Fig. 1 XANES spectra recorded at the (a) Ni (b) Fe and (c) Cr K-edges and the enlarged view of the corresponding pre-edge region observed at the (d) Ni (e) Fe and (f) Cr K-edges for both $x = 0$ and 0.2.

K-edges, respectively.^{39–41} In contrast, in $\alpha\text{-Fe}_2\text{O}_3$, where the Fe^{3+} ion resides in a regular B site, a very weak pre-edge peak has been reported.^{42,43} The second most intense pre-edge peak is observed at Ni K-edge ($x = 0$) with the peak intensity of 0.0772 (6). Similar pre-edge feature has been reported for the Ni^{2+} ion occupying the A site.⁴⁴ Thus, the intensity of the pre-edge peak indicates that the Ni^{2+} ion occupies the A site as in NiO where the Ni^{2+} ion occupies the B sites, a very weak pre-edge peak at the Ni K-edge has been reported.^{32,44} Interestingly, with the substitution of Fe in the NiCr_2O_4 lattice, the intensity of the pre-edge peak is found to decrease from 0.0772 (6) to 0.054 (8), accompanied by a very small shift in the centroid position towards higher energy (Fig. 2). It has been reported that at the Ni K-edge, the intensity of the pre-edge peak decreases with the increase in the coordination number and the pre-edge energy also shifts. Hence, the results at the Ni K-edge for $x = 0.2$ imply that a fraction of Ni^{2+} ions also occupy the B-site.^{32,44} At the Cr K-edge for $x = 0$, the pre-edge feature apparently consists of three less intense pre-edge peaks depicted as peaks A, B, and C, as shown in Fig. 2. The pre-edge peaks A and B correspond to the electric quadrupole transition of 1s electron to the t_{2g} and e_g orbitals, respectively.^{33,45} While the pre-edge peaks A and B are related to the transitions loca-

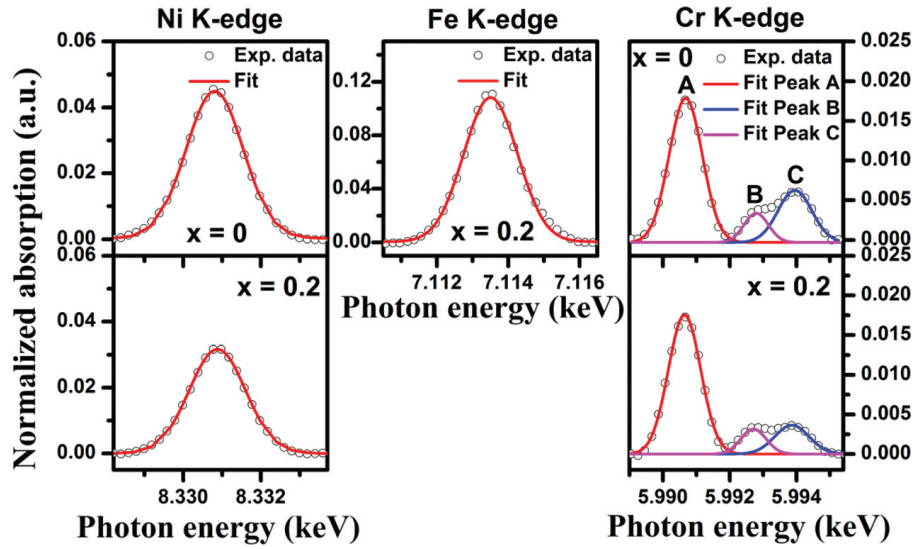


Fig. 2 Background subtracted normalized pre-edge peak along with the fitting at the Ni, Cr, and Fe K-edges for both $x = 0$ and 0.2 .

Table 1 Pre-edge peak information for $x = 0$ and 0.2 at the Ni K-edge

Sample	Normalized height	Centroid (eV)	FWHM (eV)	Peak intensity	R^2
$x = 0$	0.0446 (2)	8330.819 (4)	1.732 (7)	0.0772 (6)	0.9989
$x = 0.2$	0.0316 (1)	8330.878 (3)	1.709 (9)	0.054 (8)	0.9995

Table 2 Pre-edge peak information for $x = 0.2$ at the Fe K-edge

Sample	Normalized height	Centroid (eV)	FWHM (eV)	Peak intensity	R^2
$x = 0.2$	0.108 (2)	7113.505 (7)	1.786 (2)	0.192 (3)	0.9973

lized at the Cr absorber itself, the peak C is related to the excitation of the neighboring atoms such as (Ni/Cr/Fe).⁴⁵ These pre-edge features at the Cr K-edge are in accordance with the

trivalent Cr ion occupying the B site.⁴⁵ At $x = 0.2$, no significant change in the peaks A and B are observed, which strongly demonstrate the occupancy of Cr^{3+} ions at the B site. However, the reduction in the intensity of peak C could be due to some structural or electronic change beyond the nearest neighbor oxygen shell.⁴⁵ The qualitative analysis of FT EXAFS spectra (ESI^\dagger) also agrees with the analysis of the pre-edge region. Further, we have performed the fitting of Fourier Transformed (FT) EXAFS spectra using theoretical models based on the pre-edge peak analysis.

After qualitative analysis of the local structure around Ni^{2+} , Fe^{3+} , and Cr^{3+} ions using the XANES spectra, the fitting of the FT EXAFS spectra was performed to further consolidate and quantify the XANES spectral analysis. The k -range of the EXAFS spectra over which the Fourier transformation was performed is given in Table 4. The fitting of the FT EXAFS spectra is performed over a range of 1–4 Å at each transition metal

Table 3 Pre-edge peak information for $x = 0$ and 0.2 at the Cr K-edge

Sample	Peak	Normalized height	Centroid (eV)	FWHM (eV)	Peak intensity	R^2
$x = 0$	A	0.0178 (2)	5990.681 (5)	1.17 (1)	0.0208 (4)	0.9975
	B	0.0033 (3)	5992.795 (49)	0.86 (9)	0.0028 (5)	0.9975
	C	0.0062 (3)	5993.952 (34)	1.21 (8)	0.0075 (8)	0.9975
$x = 0.2$	A	0.0175 (1)	5990.675 (4)	1.14 (1)	0.0199 (2)	0.9982
	B	0.0032 (2)	5992.751 (45)	0.89 (8)	0.0028 (4)	0.9982
	C	0.0036 (1)	5993.881 (51)	1.21 (7)	0.0043 (3)	0.9982

Table 4 EXAFS statistical results for $x = 0$ and 0.2 at the Ni, Cr, and Fe K-edges

Sample	K-edge	k -Range (\AA^{-1})	R -Range (\AA)	N_{idp}	N_{p}	R -Factor	χ^2_{v}
$x = 0$	Cr	3.0–13.75	1.0–4.0	18.18	9	0.007	211.97
	Ni	2.8–13.4	1.0–4.0	17.30	9	0.012	384.24
$x = 0.2$	Cr	3.0–13.75	1.0–4.0	18.18	9	0.007	169.27
	Ni	2.8–13.4	1.0–4.0	17.30	12	0.011	404.73
	Fe	3.0–14.0	1.0–4.0	17.47	9	0.012	384.24

K-edge. The theoretical models used to fit the experimental spectra were developed by running the *ab initio* calculations using the FEFF6 inbuilt into the Artemis program.³¹ Structural information such as atomic coordinates, lattice, and oxygen parameters obtained from the Rietveld refinement of the XRD data was employed as the input to create the FEFF file. At the Cr K-edge, a theoretical model was used to fit the FT EXAFS spectra of $x = 0$ and 0.2 where the Cr absorber atom was considered to strictly occupy the B site (hereafter denoted as Cr_B) with the Ni scatterer atom at the A site (hereafter denoted as Ni_A). At the Fe K-edge, the FT EXAFS spectra was fitted with a theoretical model where the Fe absorber atom strictly occupied the A site (hereafter denoted as Fe_A) with the Cr_B scatterer atom. At the Ni K-edge, a theoretical model was used to fit the FT EXAFS spectrum of $x = 0$ with the Ni_A absorber atom and the Cr_B scatterer atom. For $x = 0.2$, two theoretical models were used simultaneously to fit the spectra. In the first model, Ni_A is the absorber atom with Cr_B as the scatterer atom, while in the second model, the Ni absorber atom strictly occupies the B site (hereafter denoted as Ni_B) with the Ni_A scatterer atom. Similar to that for $x = 0$ at the Ni K-edge, the FT EXAFS spectrum for $x = 0.2$ was also fitted considering Ni_A as the absorber atom; however, both the EXAFS statistical and fitting results (Tables S1 and S2†) are significantly poor compared to χ^2_v and R -factor values obtained while considering the partial occupancy of the Ni absorber atom at both the A and B sites.

The fitting of the FT EXAFS spectra was performed without any photoelectron scattering phase-shift correction for both $x = 0$ and 0.2. The amplitude reduction factor (S_0^2), an element specific quantity, is determined from the reference sample and estimated to be 0.9, 0.88, and 0.74 at the Ni, Cr, and Fe K-edges, respectively. The S_0^2 parameter is kept fixed for each path during the fitting at all the three transition metals K-edges. The Fermi energy correction (E_0) parameter was constrained to the same for each path and varied during the refinement. At $x = 0$, other EXAFS parameters such as coordi-

nation number (N), bond-length (R), and Debye-Waller factor (σ^2) were varied during the fitting. At $x = 0.2$, the same strategy was applied to fit the FT EXAFS spectra at the Cr and Fe K-edges. At the Ni K-edge, a different strategy was used to fit the FT EXAFS spectra. In this strategy, to vary N , the proportion of absorber atom in the A site is considered to be x , so the proportion of the absorber atom in the B site would be $(1 - x)$. Consequently, the number of oxygen scatterers in the first coordination shell of the A and B sites would be $4x$ and $6(1 - x)$. So, by refining the x , one can determine the N corresponding to the first coordination shell of the A and B sites. Similarly, the number of scatterers for the outer coordination shells can also be defined in terms of x and these relationships were set as a constraint. To reduce the number of fitting variables, σ^2 was constrained to be the same for the Ni-O single scattering path corresponding to the first coordination shell of the A and B sites. No constraint was applied for the parameter R and σ^2 (Ni-absorber/scatterer (metal)) and they were varied independently for each path. Fig. 3–5 shows the fitting of the EXAFS spectra in the k -space (\AA^{-1}) and magnitude and real part of the R -space (\AA) at all the three transition metals K-edges. It should also be noted that only the single scattering paths were used for the fitting of the FT EXAFS spectra. As the inclusion of multiple scattering paths led to an increase in the reduced χ^2 (χ^2_v) and the residual factor (R -factor) as well as large statistical correlation between the fitted parameters, they were not used in the presented fitting. The EXAFS statistical results and best fitting parameters obtained are tabulated in Tables 4 and 5–7, respectively. From Table 5, we find that at the Cr K-edge, no significant change in the bond length (R) and Debye-Waller (σ^2) factor was observed with the incorporation of Fe in the NiCr₂O₄ lattice. The Cr_B-O bond length of 1.985 (5)–1.990 (5) \AA obtained from the fitting was consistent with the Cr_B-O bond length of 1.987–1.990 \AA reported for NiCr₂O₄ and CoCr₂O₄.^{46,47} Similarly, at the Ni K-edge, no significant change in the Ni_A-O bond length corresponding to

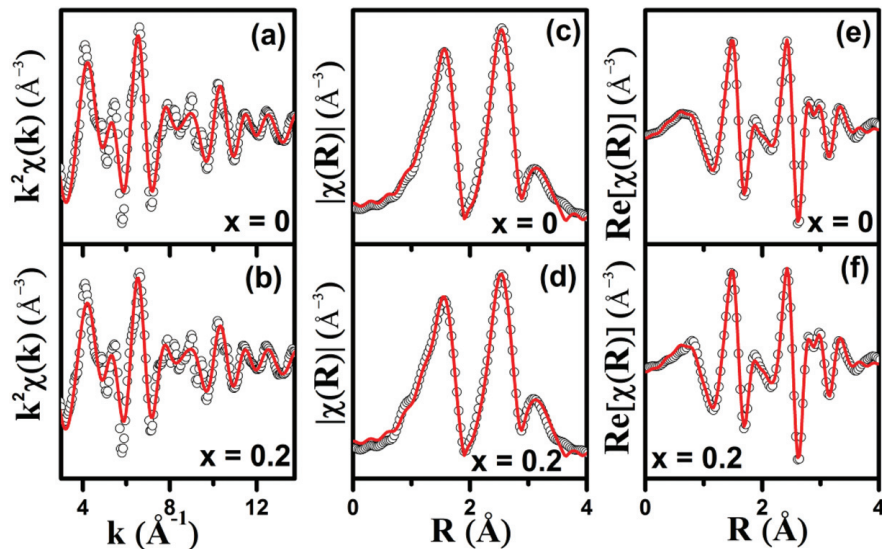


Fig. 3 Fitting of the EXAFS spectra with the theoretical pattern in (a and b) k -space (\AA^{-1}) (c and d) magnitude part of R -space (\AA) and (e and f) real part of R -space (\AA) with k^2 -weighting at the Cr K-edge for both $x = 0$ and 0.2.

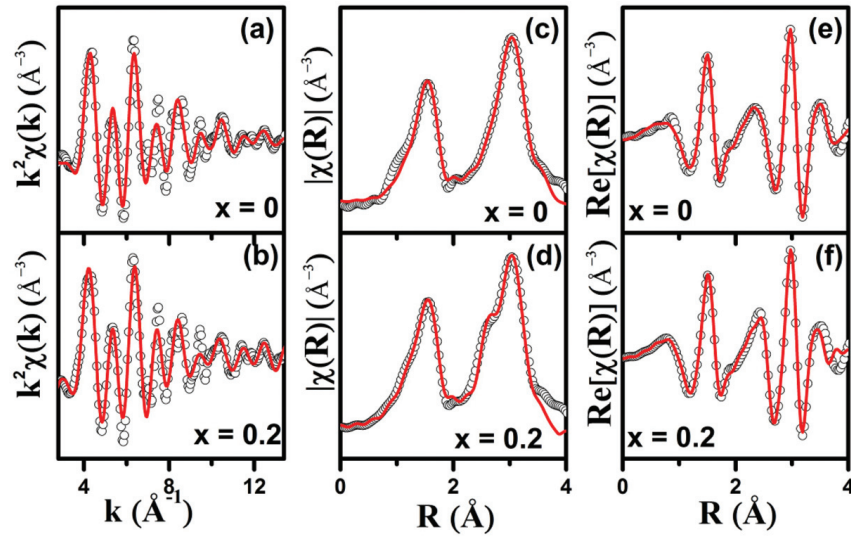


Fig. 4 Fitting of the EXAFS spectra with the theoretical pattern in (a and b) k -space (\AA^{-1}) (c and d) magnitude part of R -space (\AA) and (e and f) real part of R -space (\AA) with k^2 -weighting at the Ni K-edge for both $x = 0$ and 0.2 .

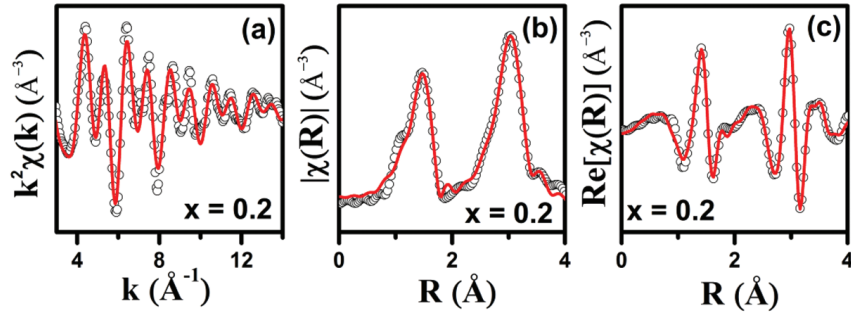


Fig. 5 Fitting of the EXAFS spectra with the theoretical pattern in (a) k -space (\AA^{-1}) (b) magnitude part of R -space (\AA) and (c) real part of R -space (\AA) with k^2 -weighting at the Fe K-edge for $x = 0.2$.

Table 5 Fitting results of the FT EXAFS spectra at the Cr K-edge for $x = 0$ and 0.2

Path	Parameter	$x = 0$	$x = 0.2$
Cr-O	N (6)	5.98 (20)	5.96 (20)
	ΔE_0 (eV)	2.14 (77)	1.03 (79)
	R (\AA)	1.990 (5)	1.985 (5)
	σ^2 (\AA^2)	0.0039 (4)	0.0035 (4)
Cr-Cr	N (6)	5.98 (20)	5.96 (20)
	ΔE_0 (eV)	2.14 (77)	1.03 (79)
	R (\AA)	2.935 (5)	2.936 (5)
	σ^2 (\AA^2)	0.0040 (3)	0.0039 (3)
Cr-Ni	N (6)	5.98 (20)	5.96 (20)
	ΔE_0 (eV)	2.14 (77)	1.03 (79)
	R (\AA)	3.455 (14)	3.454 (5)
	σ^2 (\AA^2)	0.010 (1)	0.011 (1)
Cr-O	N (6)	5.98 (20)	5.96 (20)
	ΔE_0 (eV)	2.14 (77)	1.03 (79)
	R (\AA)	3.747 (16)	3.746 (15)
	σ^2 (\AA^2)	0.0041 (4)	0.0037 (4)

the nearest neighbors of oxygen atoms was observed with the incorporation of Fe in the NiCr_2O_4 lattice (Table 6). The $\text{Ni}_A\text{-O}$ bond length of 1.946 (14)–1.950 (1) \AA obtained from the fitting was consistent with the $\text{Ni}_A\text{-O}$ bond length of 1.96 (1) \AA reported for bulk NiCr_2O_4 .^{44,46} However, in addition to the Ni_A absorber atom in $x = 0.2$, the Ni_B absorber atom also contributed to the first shell of the FT EXAFS spectra with the bond length of 2.017 (25) \AA . A significant decrease in the coordination number of the nearest neighbor oxygen atoms surrounding the Ni_A and Ni_B absorber atoms was consistent with the XANES analysis at the Ni K-edge and confirmed the distribution of Ni absorber atoms among the A and B sites. Beyond the first coordination shell of the oxygen atoms, both the bond length and σ^2 decreased with the incorporation of Fe in the NiCr_2O_4 lattice. At the Fe K-edge in $x = 0.2$, the $\text{Fe}_A\text{-O}$ bond length of 1.879 (5) \AA (Table 7) was significantly smaller than that of $\text{Cr}_B\text{-O}$ (1.985 (5)–1.990 (5) \AA) and $\text{Ni}_{A/B}\text{-O}$ (1.946 (14)–2.017 (25) \AA), which is ascribed to the relatively smaller radius of Fe^{3+} ions (0.49 \AA) in the A site. Similar to our observation, Giusta *et al.* and others have also reported a similar bond length of 1.88 \AA for Fe^{3+} ions occupying the A site environment

Table 6 Fitting results of the FT EXAFS spectra at the Ni K-edge for $x = 0$ and 0.2

Path	Parameter	$x = 0$	$x = 0.2$
Ni _A -O	N (4)	3.97 (21)	3.08 (18)
	ΔE_0 (eV)	-1.91 (139)	-1.15 (156)
	R (Å)	1.950 (1)	1.946 (14)
	σ^2 (Å ²)	0.0049 (7)	0.0046 (6)
Ni _B -O	N (6)	—	1.37 (6)
	ΔE_0 (eV)	—	-1.15 (156)
	R (Å)	—	2.017 (25)
	σ^2 (Å ²)	—	0.0046 (6)
Ni _B -Ni _B	N (6)	—	1.37 (6)
	ΔE_0 (eV)	—	-1.15 (156)
	R (Å)	—	2.960 (17)
	σ^2 (Å ²)	—	0.0060 (17)
Ni _A -Cr	N (12)	11.91 (65)	9.25 (50)
	ΔE_0 (eV)	-1.91 (139)	-1.15 (156)
	R (Å)	3.491 (8)	3.479 (10)
	σ^2 (Å ²)	0.0066 (6)	0.0046 (6)
Ni _A -O	N (12)	11.91 (65)	9.25 (50)
	ΔE_0 (eV)	-1.91 (139)	-1.15 (156)
	R (Å)	3.522 (16)	3.478 (24)
	σ^2 (Å ²)	0.0053 (6)	0.0048 (6)
Ni _A -Ni _A	N (12)	3.97 (21)	3.08 (18)
	ΔE_0 (eV)	-1.91 (139)	-1.15 (156)
	R (Å)	3.644 (13)	3.610 (16)
	σ^2 (Å ²)	0.0042 (10)	0.0026 (10)

Table 7 Fitting results of the FT EXAFS spectra at the Fe K-edge for $x = 0.2$

Path	Parameter	$x = 0.2$
Fe-O	N (4)	3.96 (19)
	ΔE_0 (eV)	-1.44 (65)
	R (Å)	1.879 (5)
	σ^2 (Å ²)	0.0031 (7)
Fe-Cr	N (12)	11.88 (57)
	ΔE_0 (eV)	-1.44 (65)
	R (Å)	3.448 (7)
	σ^2 (Å ²)	0.0050 (6)
Fe-O	N (12)	11.88 (57)
	ΔE_0 (eV)	-1.44 (65)
	R (Å)	3.775 (25)
	σ^2 (Å ²)	0.0116 (36)
Fe-Fe	N (4)	3.96 (19)
	ΔE_0 (eV)	-1.44 (65)
	R (Å)	3.576 (20)
	σ^2 (Å ²)	0.0058 (19)

of oxygen atoms.^{48,49} Hence, based on both qualitative and quantitative analysis of the XAFS spectra, we confirm that the incorporation of Fe in the NiCr₂O₄ lattice results in the occupation of the A site by the Fe³⁺ ions and the distribution of Ni²⁺ ions among the A and B sites while maintaining the preferential occupation of Cr³⁺ ions in the B sites. Further, the effect of cation distribution was examined for its structural modification prospect.

Structural and microstructural analysis

The X-ray diffraction patterns of NiCr₂O₄ and Fe doped NiCr₂O₄ at RT are shown in Fig. 6(a and b). The prominent Bragg peaks correspond to the (1 1 1), (2 2 0), (3 1 1), (2 2 2), (4 0 0), (4 2 2), (5 1 1), and (4 4 0) planes of the cubic phase of NiCr₂O₄ with the space group, $Fd\bar{3}m$ (JCPDS file no. 896615). No characteristic Bragg peaks corresponding to the impurity phases were detected within the resolution limit of XRD, which eliminates the possibility of formation of any impurity phase in both the samples. It is worth mentioning that although the tetragonal phase was observed in bulk NiCr₂O₄ at RT, we could stabilize the cubic phase at RT both with and without the incorporation of Fe in the NiCr₂O₄ lattice. Similarly, Ptak *et al.* and others also reported the decrease in cooperative J-T driven cubic to tetragonal structural phase transition temperature with the reduction in particle size of NiCr₂O₄.^{50,51} As the XAS analysis shows that the cation distribution in $x = 0$ is no different from its bulk counterpart, this suggests that the stabilization of the cubic phase at RT in the NiCr₂O₄ nanoparticles could be due to increased lattice strain with the reduction in particle size. In this context, an “internal stress model” proposed by Buessem *et al.* suggests that in a strained nanoparticle system, the system would tend to suppress the effect of spontaneous structural deformation and compel the structure towards a higher symmetry state.⁵² Thus, the structural phase transition temperature decreases with the decrease in the particle size.^{52,53} Therefore, to investigate the role of particle size and lattice strain for the cubic phase at RT, the Williamson-Hall method is employed as shown in Fig. 6(c and d). The average crystallite size and lattice strain are extracted from the XRD peak broadening using

$$\beta \cos \Theta = \frac{k\lambda}{D} + 4\varepsilon \sin \Theta \quad (1)$$

where β is the full width at half maximum (FWHM in radians), Θ is the Bragg angle, ε is the lattice strain, D is the crystallite size, and λ is the wavelength of the X-rays. The fitting results such as lattice strain and crystallite size are tabulated in Table 8. We observe that with the incorporation of Fe in the NiCr₂O₄ lattice, the lattice strain decreases and the crystallite size increases. The result clearly suggests that while the large lattice strain in the NiCr₂O₄ nanoparticles stabilizes the cubic phase at RT, at $x = 0.2$, the cubic phase at RT is due to the distribution of J-T active Ni²⁺ ions as confirmed from the XAS analysis. Further, we have carried out the scanning electron micrographs for $x = 0$ and 0.2 , as shown in Fig. 7(a) and (b), respectively. The particles are well distributed and cuboidal in shape. The particle size histograms depicted in the inset of Fig. 7 illustrate the average particle size of ~ 80.2 (3) and ~ 83.5 (2) nm for $x = 0$ and 0.2 , respectively. The Rietveld refinement is employed to fit the XRD patterns using the standard FullProf program as shown in Fig. 6.⁵⁴ The experimental, calculated, and their difference pattern are denoted as a solid line, dot, and continuous bottom line, respectively. The position of the Bragg reflections represented by the tick marks

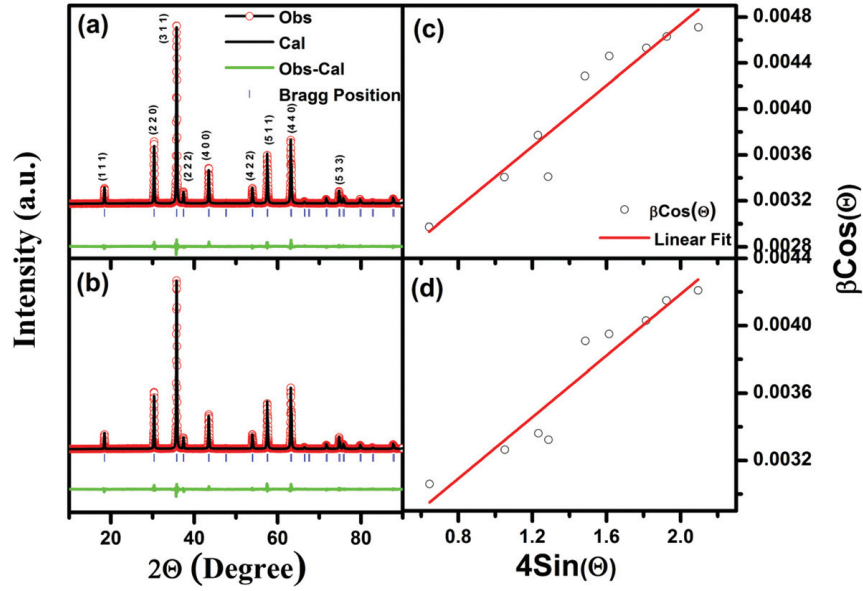


Fig. 6 Room temperature X-ray diffraction pattern of (a) $x = 0$ and (b) $x = 0.2$ along with the Rietveld refinement. Williamson–Hall plots for (c) $x = 0$ and (d) $x = 0.2$.

Table 8 Structural parameters obtained from the Williamson–Hall plot and Rietveld refinement

Sample	Crystallite size (nm)	Particle size (nm)	Lattice strain ($\epsilon \times 10^{-3}$)	Lattice parameter (\AA)
$x = 0$	58 (4)	80.2 (3)	1.33 (15)	8.3182 (1)
$x = 0.2$	66 (3)	83.5 (2)	0.84 (10)	8.3226 (1)

above the difference pattern indicate the reflection planes of the cubic phase. The lattice parameter obtained from the refinement is found to be 8.3182 (1) \AA and 8.3226 (1) \AA for $x = 0$ and 0.2, respectively. The increase in the lattice parameter corroborates with the increase in particle size and EXAFS analysis, confirming that Fe^{3+} (0.49 \AA) ions occupy the A site and replace Ni^{2+} (0.55 \AA) ions in the B site. The large radius of Ni^{2+} ion (0.69 \AA) compared to that of Cr^{3+} ion (0.61 \AA) in the B site leads to an increase in the lattice parameter.

Temperature-dependent magnetization

Fig. 8(a) and (b) illustrates the temperature dependent zero-field-cooled (ZFC) and field-cooled (FC) magnetization with an external applied field of 0.1 kOe for $x = 0$ and 0.2, respectively. With decreasing temperature from 300 K, both M_{ZFC} and M_{FC} showed an abrupt jump at about 71 K for $x = 0$, which is an indication of *para* to long-range ferrimagnetic transition temperature, T_C . T_C was estimated by fitting the linear part of M_{ZFC} and extrapolating it to zero at the temperature axis (Fig. 8). T_C was estimated to be ~ 71.2 (13) K, which is ~ 6 K higher than the $T_C \sim 65$ K of bulk NiCr_2O_4 .⁷ Further, we observed that with incorporation of 20 at% Fe in the NiCr_2O_4 lattice, T_C significantly increased to 192 (2) K which

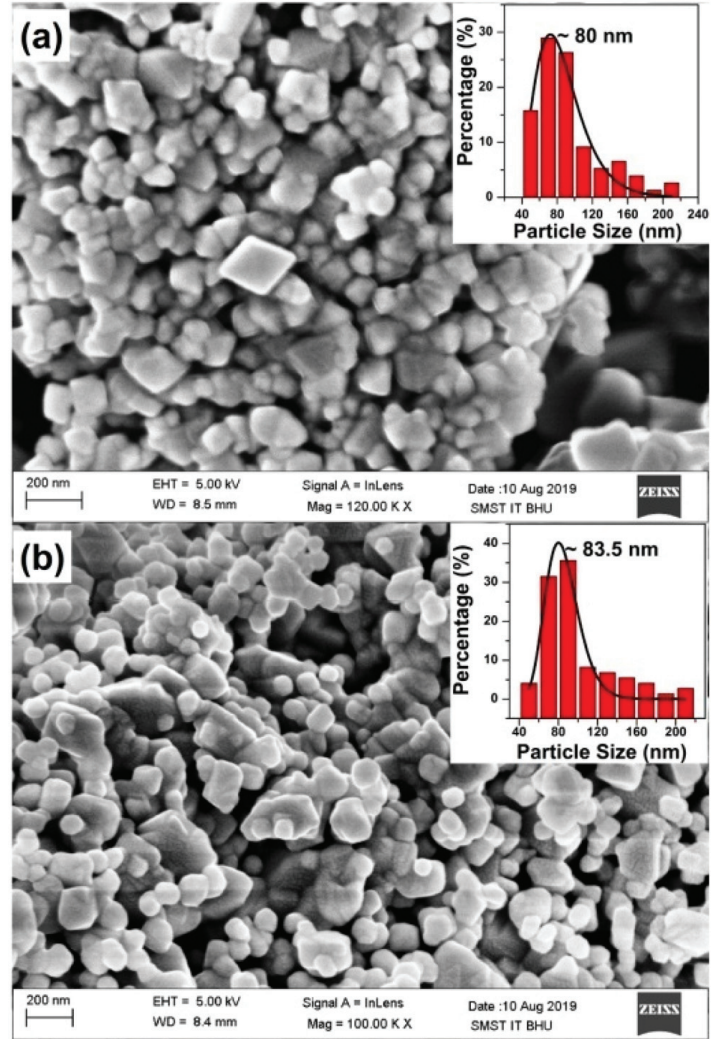


Fig. 7 Scanning electron microscope (SEM) images of (a) $x = 0$ and (b) $x = 0.2$. Particle size distribution of $x = 0$ and 0.2 are shown in the insets of panel (a) and (b), respectively.

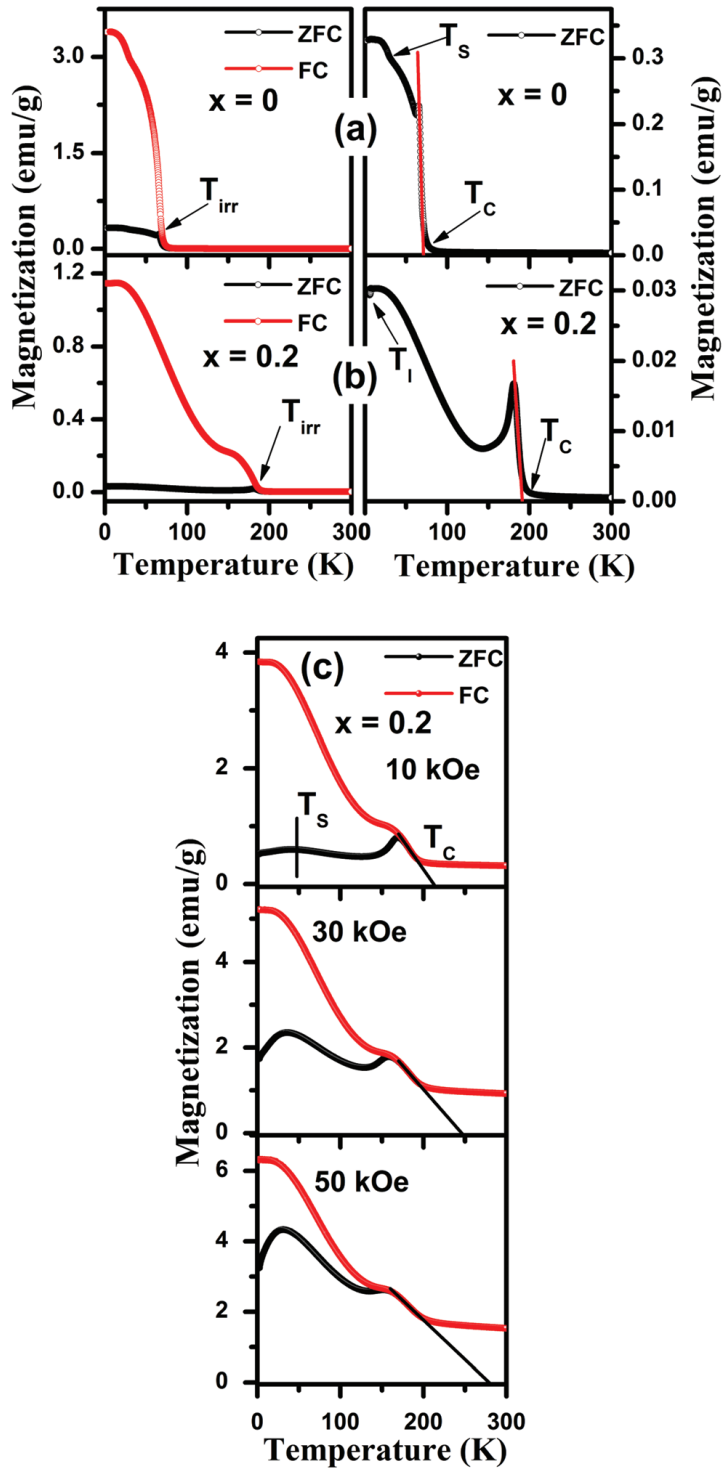


Fig. 8 Temperature dependence of magnetization under the ZFC and FC mode measured at 0.1 kOe for (a) $x = 0$ and (b) $x = 0.2$. (c) Temperature dependence of magnetization under the ZFC and FC mode measured at 10, 30, and 50 kOe for $x = 0.2$.

is much higher than that of $x = 0$. Similar to our results, Park *et al.* have reported an increase in T_c with the incorporation of 10, 30, and 50 at% Fe in the NiCr_2O_4 lattice to 135, 230, and 375 K, respectively, while the incorporation of non-magnetic Al ion in the NiCr_2O_4 lattice has been reported to exhibit a decrease in T_c due to weakening of the A-B exchange interaction.^{29,55} As T_c is governed by the strength of A-B exchange interaction, an increase in the T_c in the present case thus confirms the enhancement in the strength of A-B

exchange interaction with the incorporation of Fe ions in the NiCr_2O_4 lattice.⁵⁵ Moreover, T_c is also increased with lattice expansion in the spinel oxide nanoparticles.⁵⁶ A significant increase in the T_c of CoCr_2O_4 , MnCr_2O_4 , and MnFe_2O_4 nanoparticles from their bulk counterparts have been reported by various researchers and have been attributed to lattice expansion in the nanoparticles.^{47,56,57} Below T_c , irreversibility between M_{ZFC} and M_{FC} curves was observed at 68 K and 188 K for $x = 0$ and 0.2, respectively, which is known as irreversible temperature, T_{irr} (Fig. 8). A relatively large enhancement in M_{FC} as well as large bifurcation between M_{FC} and M_{ZFC} curves below T_{irr} implies the presence of uncompensated moments caused by strong magnetocrystalline anisotropy.⁵⁸ On further decreasing the temperature, another magnetic anomaly was observed at 28 K for $x = 0$, which is known as the spin spiral ordering temperature, T_s . T_s does not change compared to the value found in bulk NiCr_2O_4 .^{8,10} On cooling to lower temperatures, $x = 0.2$ exhibits a magnetic anomaly in the M_{ZFC} curve known as the lock-in transition temperature, T_l at about 7 K, which could not be clearly observed in $x = 0$. While T_l has been observed in bulk CoCr_2O_4 and MnCr_2O_4 at 13 and 14 K, respectively, we did not observe T_l in Fe doped CoCr_2O_4 .^{47,59} Though T_s could not be clearly observed at lower applied field (0.1 kOe) in $x = 0.2$ (Fig. 8(b)), at higher applied fields, *i.e.*, 10, 30, and 50 kOe, the presence of a broad maximum below T_c in M_{ZFC} gives the signature of T_s , as shown in Fig. 8(c). Further, we performed the neutron diffraction with XYZ polarization analysis to clearly illustrate the presence of magnetic anomalies such as T_s and T_l in $x = 0$ and 0.2.

Diffuse neutron scattering

Diffuse neutron scattering (DNS) with XYZ polarization analysis distinctively separates the contribution of spin-incoherent, magnetic, and nuclear coherent components, providing better opportunity to clearly illustrate the peculiar magnetic transitions such as T_s and T_l , which are otherwise difficult to deduce from the volume averaged macroscopic magnetic measurements. Fig. 9 shows the separated scattering contribution of spin-incoherent, magnetic, and nuclear coherent components obtained for $x = 0$ and 0.2 at 3.5 K. The intensity of spin-incoherent scattering component is almost constant in both the samples, indicating successful separation and reference calibration. The fundamental peak (111) of the magnetic scattering component is observed at the same position as that for the Bragg reflections of the nuclear coherent scattering component. However, the intensity of (111) is significantly high compared to that of the nuclear coherent scattering component in both $x = 0$ and 0.2. In addition, magnetic satellite peaks are observed at 1.08 and 1.69 \AA^{-1} in $x = 0$, while no such peaks could be clearly resolved in $x = 0.2$. The presence of satellite peaks demonstrates the presence of spin spiral magnetic structure, which is in agreement with the magnetic structure of NiCr_2O_4 deduced from the neutron diffraction measurement.¹⁰ Similarly, the presence of satellite peaks have also been reported for CoCr_2O_4 nanoparticles and are attributed to

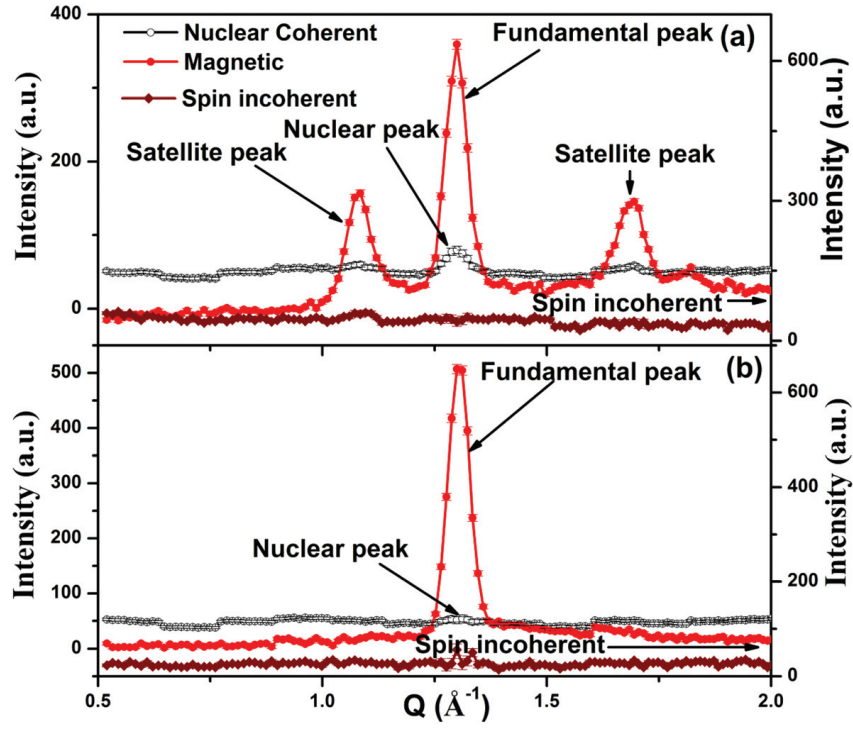


Fig. 9 Polarized neutron scattering with XYZ polarization analysis measured at 3.5 K for (a) $x = 0$ and (b) $x = 0.2$.

the spin spiral magnetic structure.^{60,61} Although, the satellite peaks cannot be clearly observed in $x = 0.2$, it does not completely rule out the presence of spin spiral magnetic structure. In 10 at% Fe doped CoCr_2O_4 nanoparticles, it has been shown that while the satellite peaks could be observed for 50 nm particles, no satellite peaks were clearly observed for 10 nm particles; however, both sizes of particles demonstrated the signature of spin spiral magnetic ordering through the temperature dependence of fundamental peak intensity.⁶² Fig. 10 shows the magnetic contributions measured in the temperature range of 3.5–80 K and 3.5–180 K for $x = 0$ and 0.2, respectively. It is clear from Fig. 10 that the fundamental magnetic peak (111) in both $x = 0$ and 0.2 broadens and diminishes towards their respective T_C , which indicates the presence of long-range ferrimagnetic ordering.⁶² In $x = 0$, transition to spin spiral magnetic ordering is accompanied by satellite peaks below 30 K in agreement with the $T_S \sim 28$ K observed macroscopically. Fig. 11 shows the variation in the integral intensity of (111) in both $x = 0$ and 0.2. Although the satellite peaks observed in $x = 0$ are absent in $x = 0.2$, the significant change in the intensity of slope of (111) at 30 and 50 K for $x = 0$ and 0.2 indicates the presence of spin spiral magnetic ordering. The tilting of magnetic moments at T_S is manifested by the variation in integral intensity of the (111) peak.⁵⁹ Further, the change in the intensity of slope of (111) observed at 7 K in $x = 0.2$ is in agreement with macroscopically observed T_I . Interestingly, while T_I could not be observed macroscopically through M vs. T plot in $x = 0$, the combined intensity of the satellite peaks clearly demonstrates the T_I at 10 K, which is also consistent with the change in the intensity of slope of (111) at 10 K. The correlation length, ξ for (111) is estimated as $\xi = \frac{2\pi}{\text{FWHM}}$, where FWHM

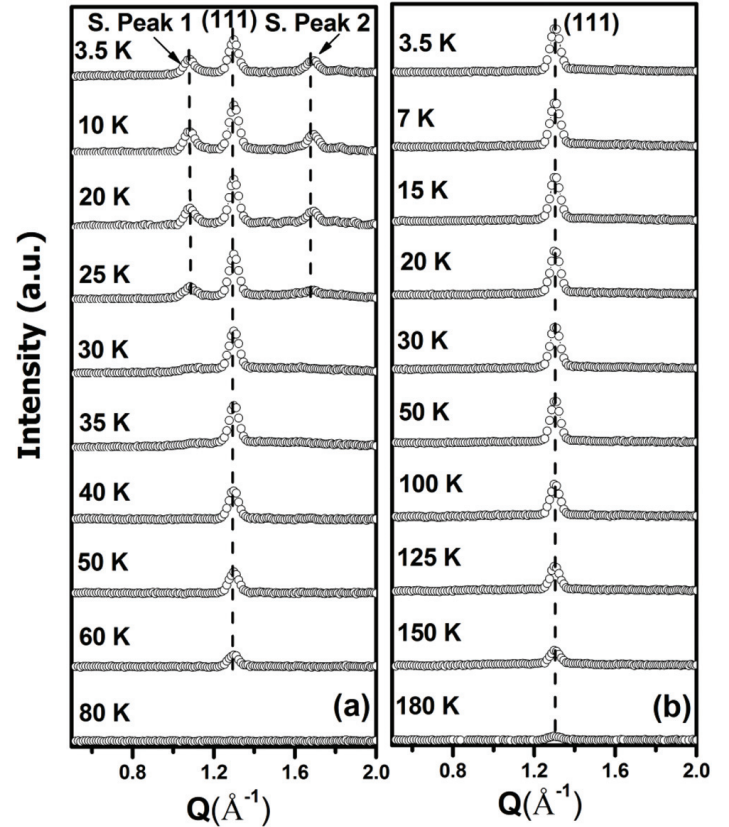


Fig. 10 Temperature dependence of magnetic component for (a) $x = 0$ and (b) $x = 0.2$ over the temperature range of 3.5–80 K and 3.5–180 K, respectively. Satellite peaks 1 and 2 are abbreviated as S. peak 1 and S. peak 2, respectively.

is the full-width at half maximum.⁶⁰ The temperature dependence of correlation length shown in Fig. 12 demonstrates that as the temperature decreases, ξ increases up to 35 and 125 K

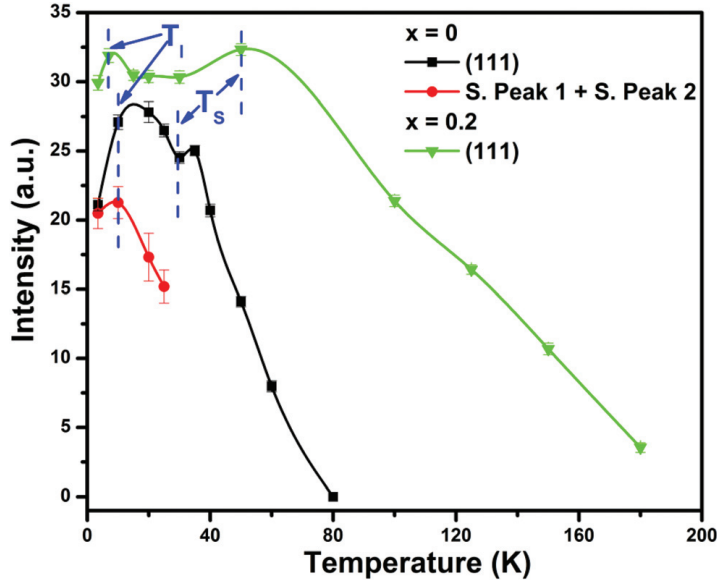


Fig. 11 Temperature dependence of the fundamental peak (111) for both $x = 0$ and 0.2 , and the combined intensity of magnetic satellite peaks for $x = 0$. Satellite peaks 1 and 2 are abbreviated as S. peak 1 and S. peak 2, respectively.

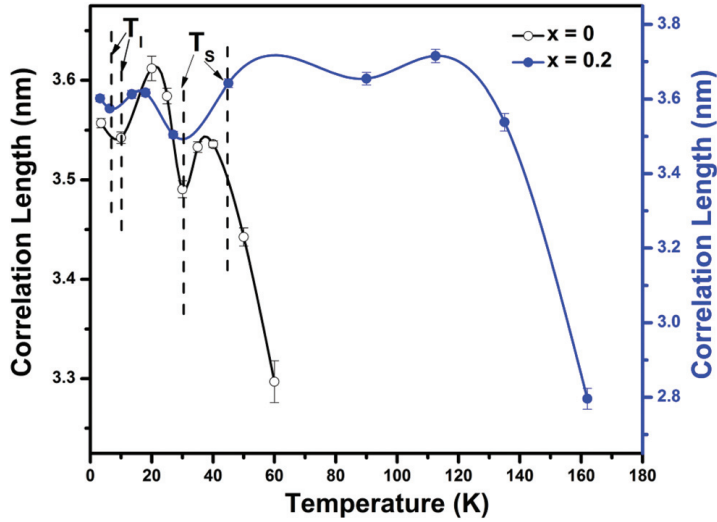


Fig. 12 Temperature dependence of the correlation length of (111) for $x = 0$ and 0.2 .

in $x = 0$ and 0.2 , respectively. On further cooling down to 3.5 K, a change in the slope is observed at 50 and 7 K for $x = 0.2$, which corroborates well with the variation in intensity of the fundamental peak (111) at T_S and T_I , respectively. Similarly, at $x = 0$, change in the slope of ξ is also observed at T_S and T_I . Moreover, ξ calculated from (111) at 3.5 K were found to be 3.557 (4) and 3.602 (9) nm for $x = 0$ and 0.2 , respectively, which are significantly smaller than their average particle size of ~ 80 nm.

Field-dependent magnetization and exchange bias

Although the crystal structure does not change with the cation distribution with the exception of the lattice parameter, magnetization measured on applying field from -70 kOe to 70 kOe

under ZFC and FC (30 kOe) conditions for $x = 0$ was very different compared to that of $x = 0.2$. Fig. 13 and 14 depict the M vs. H plot at $T = 5, 27, 35$, and 50 K for $x = 0$ and at $T = 5, 50, 70, 90, 130$, and 180 K for $x = 0.2$. In both cases, the magnetization does not saturate even after applying field up to 70 kOe.

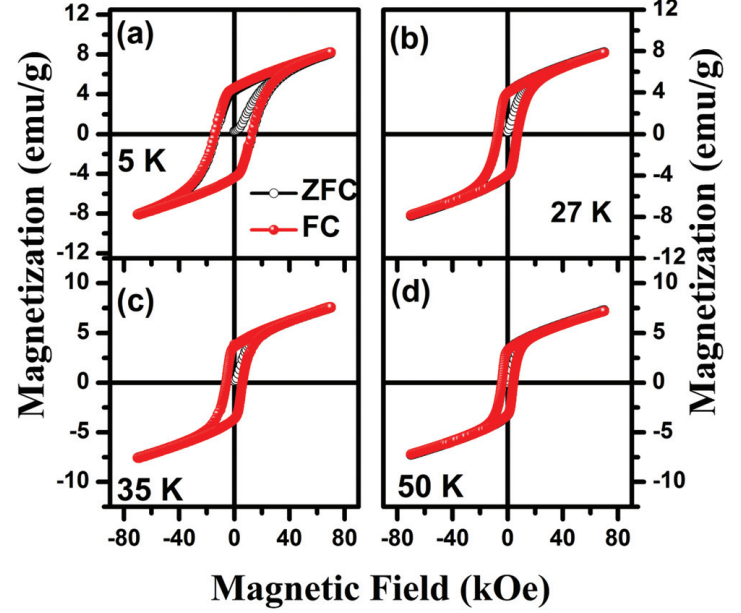


Fig. 13 Magnetic hysteresis loops measured under the ZFC and FC mode of 30 kOe at (a) 5 K (b) 27 K (c) 35 K and (d) 50 K for $x = 0$.

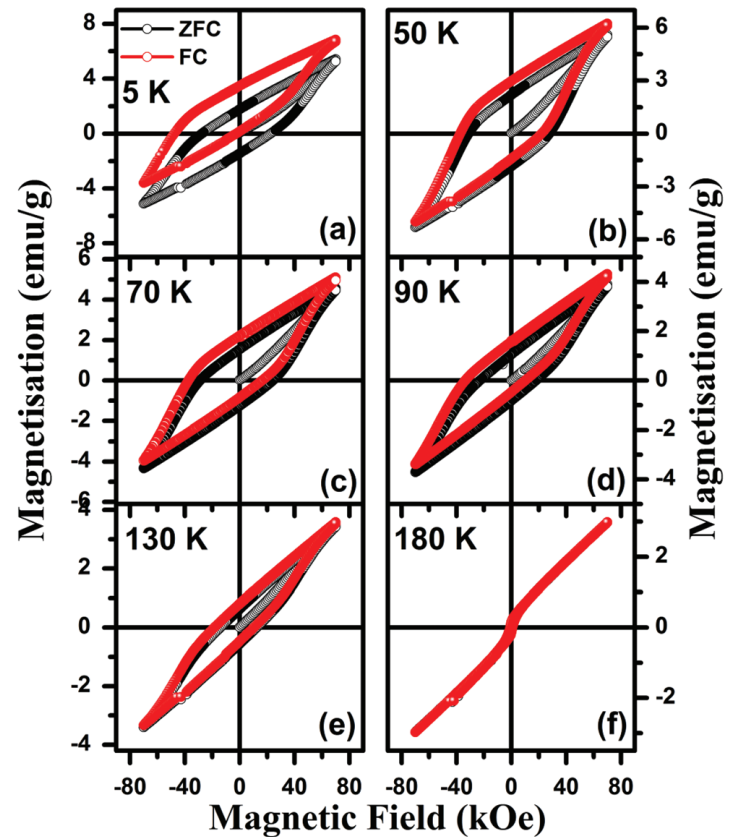


Fig. 14 Magnetic hysteresis loops measured under the ZFC and FC mode of 30 kOe at (a) 5 K (b) 50 K (c) 70 K (d) 90 K (e) 130 K and (f) 180 K for $x = 0.2$.

The non-saturation of magnetization irrespective of the measurement temperature in both the samples is ascribed to the non-collinear or canted spin structure.^{7,10} Similar to our observation, other spinel systems such as MnCr_2O_4 , NiCo_2O_4 , and NiFe_2O_4 have also been reported earlier to show non-saturation of magnetization.^{56,63,64} The magnetization at the maximum applied field, M_{max} obtained from the hysteresis loop under ZFC condition at 5 K was found to be 0.32 and $0.22\mu_{\text{B}}$ per f.u. for $x = 0$ and 0.2, respectively. Considering Néel's collinear ferrimagnetic model of two sublattices, theoretical magnetization calculated as per the cation distribution is found to be 4 and $3.2\mu_{\text{B}}$ per f.u. at 5 K for $x = 0$ and 0.2, respectively, which is an order of magnitude higher than that of M_{max} . The significant difference in magnetization further confirms the presence of non-collinear/canted spin structure.⁵⁶ Moreover, M_{max} decreases from 0.32 to $0.22\mu_{\text{B}}$ per f.u. with incorporation of Fe in the NiCr_2O_4 lattice, which could be understood based on the magnetic structure of NiCr_2O_4 proposed by Tomiyasu *et al.*¹⁰ It has been discussed that the B site is divided into two sublattices, namely, B_1 and B_2 , with their resultant moment antiparallel to the A site moment in NiCr_2O_4 . As can be observed from the EXAFS analysis, the Fe^{3+} ions occupy the A site and replace an almost equivalent amount of Ni^{2+} ions towards the B site. Thus, for the moments of B_1 and B_2 , which are antiparallel to the A site moments in NiCr_2O_4 , the moment due to B_1 sublattice aligns parallel to that of A site and antiparallel to the moment of B_2 sublattice when Fe is doped in NiCr_2O_4 . One may estimate the net magnetization per formula unit expressed as $M = \uparrow A + \uparrow B_1 - \downarrow B_2$, where $\uparrow A$, $\uparrow B_1$, and $\downarrow B_2$ are the longitudinal components of the magnetic moments of A, B_1 , and B_2 sublattices, respectively, with respect to the applied field direction. For $x = 0$, while the magnetic moment per formula unit is $4\mu_{\text{B}}$, for $x = 0.2$, the magnetic moment reduces to $2.4\mu_{\text{B}}$ due to the replacement of Ni^{2+} ions by Fe^{3+} ions in the A site and occupation of the replaced Ni^{2+} ions in the B_1 site. Moreover, M_{max} estimated from the hysteresis loop is almost an order of magnitude smaller than that of the theoretical value. This clearly implies that the spin configuration at the B site leads to a large fraction of uncompensated spins, resulting in the enhancement of non-collinearity of the spin structure, which corroborates well with the linear increase in the magnetization along the virgin curve. Fig. 15 shows the temperature dependence of coercivity, $H_C = (|H_{C1}| + |H_{C2}|)/2$, where H_{C1} and H_{C2} are coercive fields corresponding to the descending and ascending branches of the $M(H)$ loop for $x = 0$ and 0.2. Below T_C , for the $x = 0$ sample, H_C increases with decreasing temperature down to 5 K, while in the $x = 0.2$ sample, H_C increases to ~ 29 kOe with decreasing temperature down to 50 K, followed by a decrease at 5 K to ~ 25 kOe. The temperature dependence of H_C observed in $x = 0.2$ is unexpected compared to the typical trend of H_C with the temperature reported in most of the magnetic materials.^{65–68} Further, we observed that with the incorporation of Fe in the NiCr_2O_4 lattice, a drastic increase in the maximum H_C from ~ 13 to 29 kOe when x increases from 0 to 0.2 is observed. Interestingly, the H_C of 29 kOe observed in $x = 0.2$ is unusually

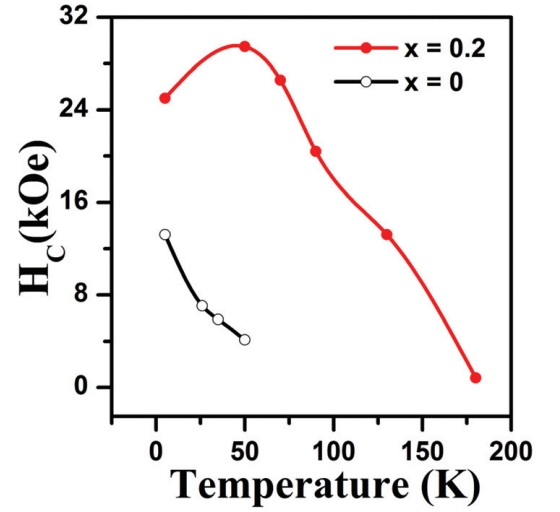


Fig. 15 Temperature dependence of H_C for $x = 0$ and 0.2 below their respective T_C .

high when compared to that of other spinel oxides and is comparable to that of rare-earth-based hard magnets.^{69–72} A large magnetocrystalline anisotropy due to the uncompensated spins leads to such high H_C and reduced M_{max} when x increases to 0.2.⁶⁷ The presence of net uncompensated spins, which do not rotate with the applied field of 70 kOe, are expected to give rise to vertical magnetization shift and unidirectional exchange anisotropy between the A and B sublattices that consequently leads to asymmetric behavior of the hysteresis loop, as observed in $x = 0.2$ under ZFC and FC conditions (Fig. 14). No such asymmetric behavior of the hysteresis loop was observed for $x = 0$, which gives an evidence of less H_C (Fig. 13). The asymmetric hysteresis loops are found to shift towards the negative field and positive magnetization axes with decreasing temperature below T_C , giving an indication of the conventional exchange bias (CEB) and spontaneous exchange bias (SEB) under FC and ZFC conditions, respectively.^{17–19} Fig. 16 shows the temperature dependence of $H_{\text{CEB/SEB}} = (H_{C1} + H_{C2})/2$ and the vertical shift of magnetization, $\Delta M^{\text{FC/ZFC}} = (M_{\text{max}}(+H) + M_{\text{max}}(-H))/2$, where $M_{\text{max}}(+H)$ and $M_{\text{max}}(-H)$ are the magnetization at the maximum applied field of 70 kOe in the positive and negative direction, respectively. As the temperature is lowered below T_C , H_{CEB} increases and exhibits a local maximum of ~ 11 kOe at 90 K. On further decreasing the temperature, at 50 K, H_{CEB} exhibits a minimum followed by an increase in the H_{CEB} to ~ 26 kOe at 5 K. The H_{CEB} of ~ 26 kOe is not only significantly larger than the previously reported H_{CEB} in similar spinel systems such as in $x = 0.1$ but is also comparable to extremely large H_{CEB} (~ 33 kOe) reported in the Mn–Pt–Ga based Heusler alloy.^{11,72} Interestingly, H_{SEB} also exhibits a temperature-dependent behavior similar to that of H_{CEB} and shows a maximum of 2.6 kOe at 5 K, which is an order of magnitude smaller than maximum the H_{CEB} (~ 26 kOe). Similar to $H_{\text{CEB/SEB}}$, the maximum ΔM^{FC} of $0.13\mu_{\text{B}}$ per f.u. observed at 5 K is found to be almost an order of magnitude higher than ΔM^{ZFC} ($\sim 0.013\mu_{\text{B}}$ per f.u.). Further, one can see clearly from Fig. 16 that the

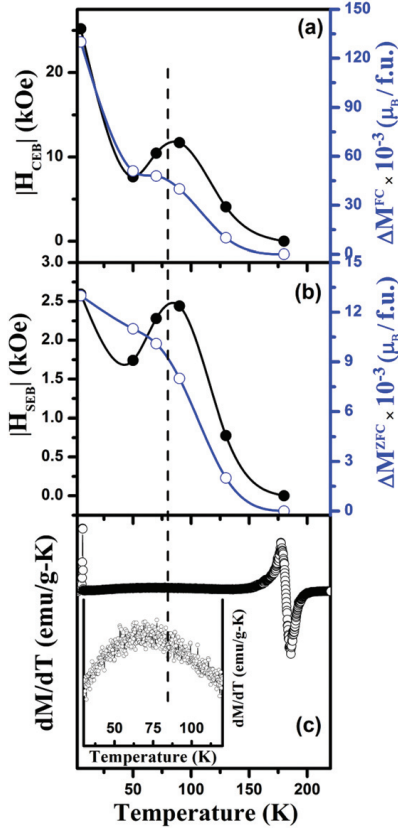


Fig. 16 Temperature dependence of (a) $H_{CEB/SEB}$ (b) $\Delta M^{FC/ZFC}$ and (c) dM_{ZFC}/dT for $x = 0.2$. Inset in panel (c) show the broad peak observed in the dM/dT vs. T plot at about 70 K.

temperature dependence of $\Delta M^{FC/ZFC}$ shows a change in the slope at 50 and 90 K, which corresponds well to the minimum and maximum observed in the temperature dependent H_{CEB}/H_{SEB} . The drop in H_{CEB}/H_{SEB} and $\Delta M^{FC/ZFC}$ at 50 K clearly shows the evidence of T_s in agreement with the DNS analysis. To understand this, the first derivative of M_{ZFC} with temperature (dM/dT) is shown in Fig. 16(c). Below T_C , dM/dT increases with decreasing temperature, showing a broad peak nearly at the same temperature where the H_{CEB}/H_{SEB} shows the maximum (inset of Fig. 16(c)). The minimum in H_{CEB}/H_{SEB} corroborates with the minimum of dM/dT , followed by an increase at T_l . Although, the temperature dependence of H_{CEB}/H_{SEB} exhibits similar temperature dependent behavior as that of dM/dT in both $x = 0.2$ and $x = 0.1$ (in our previous study), the magnitude of H_{CEB}/H_{SEB} is significantly enhanced in $x = 0.2$ compared to that of $x = 0.1$.¹¹ Moreover, similar to H_{CEB}/H_{SEB} , $\Delta M^{FC/ZFC}$ is also increased more than twice as compared to $\Delta M^{FC/ZFC}$ observed in $x = 0.1$.¹¹ As the magnitude of exchange bias field is directly correlated to the number of irreversible uncompensated spins at the B site providing pinning force to the rotation of reversible spins at the A site, almost two-fold increase in H_{CEB}/H_{SEB} in $x = 0.2$ confirms the presence of a large fraction of uncompensated spins at the B site providing large pinning effect on the rotation of reversible FM ordering at the A site. This clearly implies that uncompensated spins play a vital role in the origin of exchange bias effect. Further, we have investigated the change in the

exchange bias with the increasing number of cycles of hysteresis loop.

Training effect (T.E.) studies were performed by measuring exchange bias under 30 kOe at 5 K after repeating the hysteresis loop 6 times. It is evident from Fig. 17 that H_{C1} (Fig. 17(b)) exhibits a significantly larger shift towards the positive field axis compared to that of H_{C2} (Fig. 17(c)), which is a typical feature shown by the exchange coupled system.⁷³ It indicates that T.E. is mainly governed by the number of cycle dependence of H_{C1} . A gradual decrease in the H_{CEB} with subsequent number of cycles is observed (Fig. 17). The % of T.E. is calculated as the relative decrease in H_{CEB} with an increasing number of cycles as given below:

$$\% \text{ of T.E.} = \left(1 - \frac{H_{CEB}^1 - H_{CEB}^n}{H_{CEB}^1} \right) \times 100(\%), \quad (2)$$

where H_{CEB}^n is the exchange bias field of the n^{th} cycle.

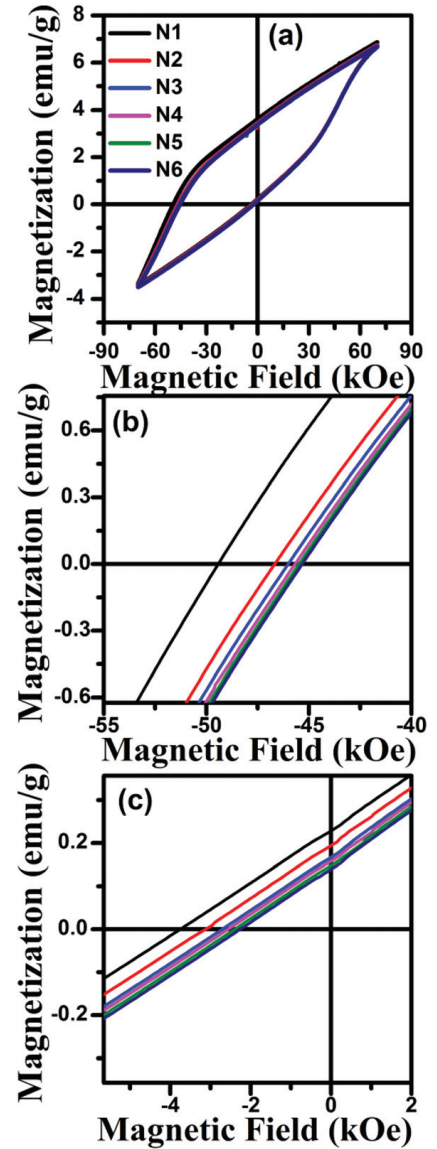


Fig. 17 (a) T.E. observed in $x = 0.2$ for a total number of six hysteresis loops. Panel (b) and (c) show the shifting of descending and ascending branches of the hysteresis loops, respectively, with the number of cycles.

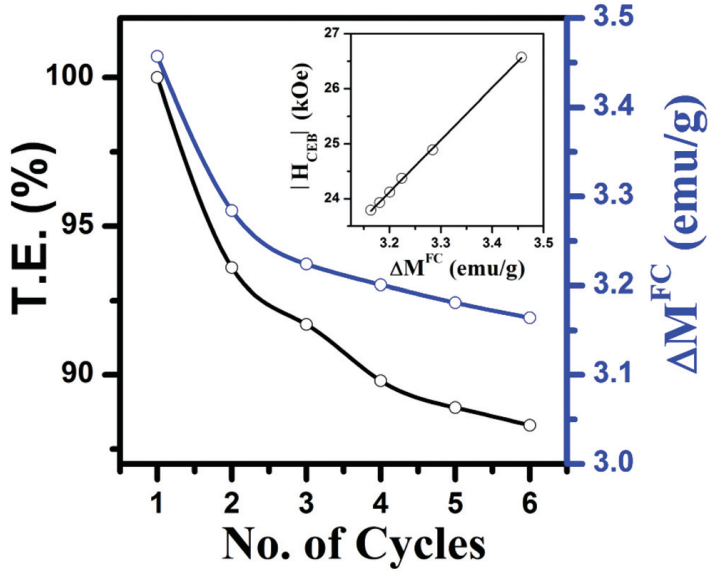


Fig. 18 Number of cycles dependence of T.E. and ΔM^{FC} for $x = 0.2$. Inset shows the linear dependence of H_{CEB} over ΔM^{FC} .

The % of T.E. and ΔM^{FC} with the number of cycles is shown in Fig. 18. One may notice that with an increasing number of cycles, T.E. decreases gradually and attains the value of 93.6% after the 1st cycle and 88.3% after the 6th cycle. Moreover, the decrease in % of T.E. between the first two cycles is 6%, which is significantly larger than the difference between the subsequent cycles, indicating faster rate of relaxation of magnetization. The % of T.E. has a similar decreasing tendency such as ΔM^{FC} with the number of cycles. In the inset of Fig. 18, a linear dependence of H_{CEB} on ΔM^{FC} is observed. This linear dependence of H_{CEB} on ΔM^{FC} suggests that both H_{CEB} and ΔM^{FC} are strongly correlated to the decrease in the number of frozen uncompensated spins upon field cycling. In order to investigate the microscopic mechanism behind the training effect, the H_{CEB} as the function of number of cycles is fitted with the following simple power law:

$$H_{\text{eb}}(n) = H_{\text{eb}}(\infty) + \kappa/\sqrt{n}. \quad (3)$$

Here, κ is the system-dependent constant and $H_{\text{eb}}(\infty)$ is the H_{CEB} in the limit of an infinite number of loops. In the fitting of experimental data with eqn (3) shown in Fig. 19, the fitted parameters $H_{\text{eb}}(\infty)$ and κ were found to be 22.29 ± 0.04 kOe and 3.65 ± 0.08 , respectively. From Fig. 19, one can clearly see that eqn (3) does not fit the experimental data very well. The possible reason could be the fact that eqn (3) considers only the change in AFM magnetization while the effect of frozen uncompensated spins at FM/AFM interface is neglected, which could also modify the AFM magnetic anisotropy at the interface.^{73,74} The modified AFM magnetic anisotropy leads to the essentially two different components of uncompensated AFM spins such as rotatable and frozen uncompensated AFM spins, which are strongly exchanged coupled to the FM and AFM layers, respectively. The frozen AFM component mostly remains unchanged in a moderate field. But some of them could also deviate at a sufficiently large applied field, resulting

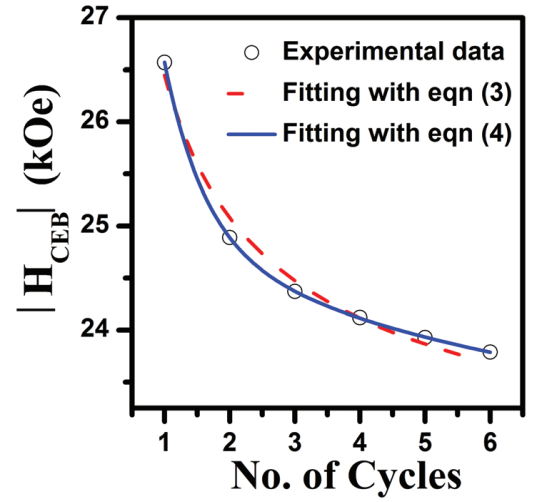


Fig. 19 Number of cycles dependence of H_{CEB} calculated from each hysteresis loop in $x = 0.2$. Experimental data are shown by the open circle while the line and dash represent the phenomenological model and simple power law, respectively.

in an irreversible change in the frozen uncompensated AFM spins. Therefore, we expect that a phenomenological model, which considers the modification in AFM anisotropy at the interface, could fit our experimental data comparatively well. In this context, we have fitted the experimental data with the following multiple exponent expression, which considers the modification in AFM anisotropy at the interface:^{73,74}

$$H_{\text{eb}}(n) = H_{\text{eb}}(\infty) + k_{\text{f}}e^{-n/\beta_{\text{f}}} + k_{\text{i}}e^{-n/\beta_{\text{i}}}. \quad (4)$$

Here, k_{f} and β_{f} are the parameters related to the change of the frozen spins, k_{i} and β_{i} are the parameters related to the interfacial magnetic frustration. The k parameter has the dimension of magnetic field (Oe) while β is dimensionless and resembles the relaxation time. One may notice that the experimental data are fitted well with the eqn (4), as shown in Fig. 19. The parameters obtained from the best fit of experimental data are $H_{\text{eb}}(\infty) = 23.02 \pm 0.42$ kOe, $k_{\text{f}} = 8.76 \pm 0.5$ kOe, $\beta_{\text{f}} = 0.61 \pm 0.05$, $k_{\text{i}} = 2.14 \pm 0.15$ kOe, and $\beta_{\text{i}} = 5.82 \pm 2.71$. The frozen uncompensated AFM spins at the interface appear to relax at a significantly slower rate than the rotatable uncompensated AFM spins, as expected.⁷⁴ The relaxation of the frozen uncompensated AFM moments with the consecutive number of cycles leads to irreversible changes in them; hence, H_{CEB} decreases.

Conclusion

In summary, we found that decreasing the particle size to the nanometer range in $\text{NiCr}_{2-x}\text{Fe}_x\text{O}_4$ ($x = 0$ and 0.2) suppressed the cooperative Jahn–Teller distortion and consequently, a stabilization of the high-temperature cubic phase ($Fd\bar{3}m$) was observed in bulk NiCr_2O_4 at RT. Through XAFS analysis, we demonstrated that the incorporation of Fe in the NiCr_2O_4 lattice resulted in the redistribution of cations among the A

and B sites where Fe^{3+} and Cr^{3+} ions occupied the A and B sites, respectively, while the Ni^{2+} ions were distributed among the A and B sites. The redistribution of cations led to the transformation of the normal spinel structure in $x = 0$ to the mixed spinel structure in $x = 0.2$. The effect of normal to mixed spinel structure transformation on the magnetic properties was analyzed through both magnetic measurements and DNS with XYZ polarization analysis. The magnetic measurement showed a significant enhancement in the T_C from 71 to 191 K in agreement with the DNS analysis. Moreover, the DNS analysis clearly demonstrated the presence of T_S and T_I in both the compositions, which were otherwise difficult to deduce from the volume averaged magnetic measurements. While T_S increased from 28 K to 50 K with the incorporation of Fe in the NiCr_2O_4 lattice, T_I decreased from 10 K to 7 K. Besides the enhancement in T_C and T_S , a drastic increase in the H_C from ~ 13 kOe to 29 kOe with the incorporation of Fe in the NiCr_2O_4 lattice was observed. The giant H_C in $x = 0.2$ was ascribed to the presence of large magneto-crystalline anisotropy accompanied by uncompensated spins at the B site. Unlike the bilayer exchange coupled systems, significantly large H_{CEB} and H_{SEB} of ~ 26 and ~ 2.6 kOe were observed in the single phase for $x = 0.2$. The pinning effect of irreversible uncompensated spins at the B site on the reversible spins at the A site was ascribed to the development of unidirectional exchange bias anisotropy and hence, high exchange bias was observed. The training effect was detected in $x = 0.2$ and was explained using the phenomenological model considering the role of irreversible uncompensated spins.

Conflicts of interest

There are no conflicts to declare.

Acknowledgements

The authors acknowledge DST, India and ICTP, Italy, for providing the funding and beam time to perform the XAFS measurements at Elettra, Trieste, Italy. The authors also acknowledge Giuliana Aquilanti for her kind assistance in carrying out the XAFS measurements. CR also acknowledges JCNS at Garching, Germany, for providing beam time to carry out the DNS measurements. The authors also acknowledge CIFIC, IIT (BHU), Varanasi, India for the magnetic measurements.

References

- W. Hu, N. Qin, G. Wu, S. Li and D. Bao, *J. Am. Chem. Soc.*, 2012, **134**, 14658.
- D. C. Kim and S. K. Ihm, *Environ. Sci. Technol.*, 2001, **35**, 222.
- Y. Yamasaki, S. Miyasaka, Y. Kaneko, J. P. He, T. Arima and Y. Tokura, *Phys. Rev. Lett.*, 2006, **96**, 207204.
- H. S. C. O'Neill and A. Navrotsky, *Am. Mineral.*, 1983, **69**, 181.
- V. Kocsis, S. Bordács, D. Varjas, K. Penc, A. Abouelsayed, C. A. Kuntscher, K. Ohgushi, Y. Tokura and I. Kézsmárki, *Phys. Rev. B: Condens. Matter Mater. Phys.*, 2013, **87**, 064416.
- M. R. Suchomel, D. P. Shoemaker, L. Ribaud, M. C. Kemei and R. Seshadri, *Phys. Rev. B: Condens. Matter Mater. Phys.*, 2012, **86**, 054406.
- T. D. Sparks, M. C. Kemei, T. Barton, R. Seshadri, E. D. Mun and V. S. Zapf, *Phys. Rev. B: Condens. Matter Mater. Phys.*, 2014, **89**, 024405.
- S. Klemme and J. C. van Miltenbur, *Phys. Chem. Miner.*, 2002, **29**, 663.
- H. Ishibashi and T. Yasumi, *J. Magn. Magn. Mater.*, 2007, **310**, e610.
- K. Tomiyasu and I. Kagomiya, *J. Phys. Soc. Jpn.*, 2004, **73**, 2539.
- G. C. Pandey, G. Aquilanti, P. U. Sastry and C. Rath, *Ceram. Int.*, 2019, **45**, 13874.
- C. Li, T. Yan, G. Zerihun, Q. Fu, R. Zhang, X. Chen, S. Huang and S. Yuan, *J. Am. Ceram. Soc.*, 2018, **101**, 5571.
- J. Barman and S. Ravi, *J. Mater. Sci.*, 2018, **53**, 7187.
- S. Gider, B. U. Runge, A. C. Marley and S. S. P. Parkin, *Science*, 1998, **281**, 797.
- C. Tsang, T. Lin, S. MacDonald, M. Pinarbasi, N. Robertson, H. Santini, M. Doerner, T. Reith, L. Vo, T. Diola and P. Arnett, *IEEE Trans. Magn.*, 1997, **33**, 2866.
- L. E. Fernandez-Outon, K. O'grady, S. Oh, M. Zhou and M. Pakala, *IEEE Trans. Magn.*, 2008, **44**, 2824.
- J. Nogués and I. K. Schuller, *J. Magn. Magn. Mater.*, 1999, **192**, 203.
- X. Wang, S. Gao, X. Yan, Q. Li, J. Zhang, Y. Long, K. Ruan and X. Li, *Phys. Chem. Chem. Phys.*, 2018, **20**, 3687.
- S. Giri, R. Sahoo, P. Dasgupta, A. Poddar and T. Nath, *J. Phys. D: Appl. Phys.*, 2016, **49**, 165002.
- W. H. Meiklejohn and C. P. Bean, *Phys. Rev.*, 1956, **102**, 1413.
- M. Ali, P. Adie, C. H. Marrows, D. Greig, B. J. Hickey and R. L. Stamps, *Nat. Mater.*, 2007, **6**, 70.
- Z. Shi, J. Du and S. Zhou, *Chin. Phys. B*, 2014, **23**, 027503.
- W. C. Cain and M. H. Kryder, *J. Appl. Phys.*, 1990, **67**, 5722.
- B. M. Wang, Y. Liu, P. Ren, B. Xia, K. B. Ruan, J. B. Yi, J. Ding, X. G. Li and L. Wang, *Phys. Rev. Lett.*, 2011, **106**, 077203.
- S. Giri, R. Sahoo, P. Dasgupta, A. Poddar and T. Nath, *J. Phys. D: Appl. Phys.*, 2016, **49**, 165002.
- P. Liao, C. Jing, X. Wang, Y. Yang, D. Zheng, Z. Li, B. Kang, D. Deng, S. Cao, J. Zhang and B. Lu, *Appl. Phys. Lett.*, 2014, **104**, 092410.
- T. Maity, S. Goswami, D. Bhattacharya and S. Roy, *Phys. Rev. Lett.*, 2013, **110**, 107201.
- L. G. Wang, C. M. Zhu, Z. M. Tian, H. Luo, D. L. G. C. Bao and S. L. Yuan, *Appl. Phys. Lett.*, 2015, **107**, 152406.
- J. Barman and S. Ravi, *J. Magn. Magn. Mater.*, 2017, **426**, 82.
- C. M. Zhu, L. G. Wang, L. Chen, D. L. G. C. Bao, M. C. Wang and S. L. Yuan, *J. Mater. Sci.*, 2016, **51**, 9415.
- B. Ravel and M. Newville, *J. Synchrotron Radiat.*, 2005, **12**, 537.

- 32 T. Yamamoto, *X-Ray Spectrom.*, 2008, **37**, 572.
- 33 G. S. Henderson, F. M. F. de Groot and B. J. A. Moulton, *Rev. Mineral. Geochem.*, 2014, **78**, 75.
- 34 Y. Joly and S. Grenier, in *X-Ray Absorption and X-Ray Emission Spectroscopy: Theory and Applications*, ed. J. A. V. Bokhoven and C. Lamberti, John Wiley & Sons, Ltd, Hoboken, New Jersey, USA, 2016, ch. 4, p. 73.
- 35 V. R. Mastelaro and E. D. Zanotto, *Materials*, 2018, **11**, 204.
- 36 J. E. Penner-Hahn, *Coord. Chem. Rev.*, 1999, **1101**, 190.
- 37 U. Kusthardt, B. Hedman, K. Hodgson, R. Hahn and H. Vilter, *FEBS Lett.*, 1993, **329**, 5.
- 38 M. Wilke, F. Farges, G. M. Partzsch, C. Schmidt and H. Behrens, *Am. Mineral.*, 2007, **92**, 44.
- 39 D. Kothari, V. R. Reddy, A. Gupta, C. Meneghini and G. Aquilanti, *J. Phys.: Condens. Matter*, 2010, **22**, 356001.
- 40 B. Ravel, E. A. Stern, R. I. Vedralinskii and V. Kraizman, *Ferroelectrics*, 1998, **206–207**, 407.
- 41 M. L. Moreira, G. P. Mambrini, D. P. Volanti, E. R. Leite, M. O. Orlandi, P. S. Pizani, V. R. Mastelaro, C. O. Paiva-Santos, E. Longo and J. A. Varela, *Chem. Mater.*, 2008, **20**, 5381.
- 42 A. Corrias, G. Ennas, G. Mountjoy and G. Paschina, *Phys. Chem. Chem. Phys.*, 2000, **2**, 1045.
- 43 P. Canepa, E. Schofield, A. V. Chadwick and M. Alfredsson, *Phys. Chem. Chem. Phys.*, 2011, **13**, 12826.
- 44 F. Farges, G. E. Brown Jr., P.-E. Petit and M. Munoz, *Geochim. Cosmochim. Acta.*, 2001, **65**, 1665.
- 45 J. Frommer, M. Nachtegaal, I. Czekaj, T. C. Weng and R. Kretschmar, *J. Phys. Chem. A*, 2009, **113**, 12171.
- 46 O. Crottaz, F. Kubel and H. Schmid, *J. Mater. Chem.*, 1997, **71**, 43.
- 47 D. Kumar, A. Banerjee, A. Mahmoud and C. Rath, *Dalton Trans.*, 2017, **46**, 10300.
- 48 A. D. Giusta, S. Carbonin and G. Ottonello, *Mineral. Mag.*, 1996, **60**, 603.
- 49 R. M. Hazen and H. Yang, *Am. Mineral.*, 1999, **84**, 1956.
- 50 M. Ptak, M. Maczka, A. Gabor, A. Pikul, L. Macalik and J. Hanuza, *J. Solid State Chem.*, 2013, **201**, 270.
- 51 A. Rathi, P. D. Babu, P. K. Rout, V. P. S. Awana, V. K. Tripathi, R. Nagarajan, B. Sivaiah, R. P. Pant and G. A. Basheed, *J. Magn. Magn. Mater.*, 2019, **474**, 585.
- 52 W. R. Buessem, L. E. Cross and A. K. Goswami, *J. Am. Ceram. Soc.*, 1966, **49**, 33.
- 53 S. Chattopadhyay, P. Ayyub, V. R. Palkar and M. Multani, *Phys. Rev. B*, 1995, **52**, 18.
- 54 J. Rodriguez-Carvajal, Fullprof: A Program for Rietveld Refinement and Pattern Matching Analysis, Abstract of the Satellite Meeting on Powder Diffraction of the XV Congress of the IUCr, Toulouse, France, 1990, p. 127.
- 55 S. I. Park and C. S. Kim, *J. Appl. Phys.*, 2007, **101**, 09N511.
- 56 R. N. Bhowmik, R. Ranganathan and R. Nagarajan, *Phys. Rev. B: Condens. Matter Mater. Phys.*, 2006, **73**, 144413.
- 57 Z. X. Tang, C. M. Sorensen, K. J. Klabunde and G. C. Hadjipanayis, *Phys. Rev. Lett.*, 1991, **67**, 25.
- 58 C. Li, T. Yan, C. Chakrabarti, R. Zhang, X. Chen, Q. Fu, S. Yuan and G. O. Barasa, *J. Appl. Phys.*, 2018, **123**, 093902.
- 59 K. Tomiyasu, J. Fukunaga and H. Suzuki, *Phys. Rev. B: Condens. Matter Mater. Phys.*, 2004, **70**, 214434.
- 60 D. Zakutna, J. Vlcek, P. Fitl, K. Nemkovski, D. Honecker, D. Niznansky and S. Disch, *Phys. Rev. B: Condens. Matter Mater. Phys.*, 2018, **98**, 064407.
- 61 D. Zakutna, A. Alemayehu, J. Vlcek, K. Nemkovski, C. P. Grams, D. Niznansky, D. Honecker and S. Disch, *Phys. Rev. B: Condens. Matter Mater. Phys.*, 2019, **100**, 184427.
- 62 D. Kumar, J. K. Galivarapu, A. Banerjee, K. S. Nemkovski, Y. Su and C. Rath, *Nanotechnology*, 2016, **27**, 175702.
- 63 J. F. Marco, J. R. Gancedo, M. Gracia, J. L. Gautier, E. I. Rios, H. M. Palmer, C. Greaves and F. J. Berry, *J. Mater. Chem.*, 2001, **11**, 3087.
- 64 E. C. Passamani, B. R. Segatto, C. Larica, R. Cohen and J. M. Greneche, *J. Magn. Magn. Mater.*, 2010, **322**, 3917.
- 65 E. Fertman, S. Dolya, V. Desnenko, L. A. Pozhar, M. Kajnakova and A. Feher, *J. Appl. Phys.*, 2014, **115**, 203906.
- 66 X. H. Huang, J. F. Ding, G. Q. Zhang, Y. Hou, Y. P. Yao and X. G. Li, *Phys. Rev. B: Condens. Matter Mater. Phys.*, 2008, **78**, 224408.
- 67 J. F. Qian, A. K. Nayak, G. Kreiner, W. Schnelle and C. Felser, *J. Phys. D: Appl. Phys.*, 2014, **47**, 305001.
- 68 S. Xu, Y. Ma, B. Geng, X. Sun and M. Wang, *Nanoscale Res. Lett.*, 2016, **11**, 471.
- 69 K. Maaz, A. Mumtaz, S. K. Hasanain and M. F. Bertino, *J. Magn. Magn. Mater.*, 2010, **322**, 2199.
- 70 P. S. A. Kumar, P. A. Joy and S. K. Date, *Bull. Mater. Sci.*, 2000, **23**, 97.
- 71 C. Prados and G. C. Hadjipanayis, *Appl. Phys. Lett.*, 1999, **74**, 430.
- 72 A. K. Nayak, M. Nicklas, S. Chadov, P. Khuntia, C. Shekhar, A. Kalache, M. Baenitz, Y. Skourski, V. K. Guduru, A. Puri, U. Zeitler, J. M. D. Coey and C. Felser, *Nat. Mater.*, 2015, **14**, 679.
- 73 S. K. Mishra, F. Radu, H. A. Durr and W. Eberhardt, *Phys. Rev. Lett.*, 2009, **102**, 177208.
- 74 F. Radu and H. Zabel, *Springer Tracts Mod. Phys.*, 2008, **227**, 97.